

# Trafficking synaptic cargo involves tradeoffs in speed and precision

Alex H. Williams<sup>1,2,3,\*</sup>, Cian O'Donnell<sup>2</sup>, Eve Marder<sup>4</sup>, Terrence Sejnowski<sup>2,5</sup>, and Timothy O'Leary<sup>4,\*</sup>

<sup>1</sup>Department of Neurosciences, University of California, San Diego, La Jolla, CA 92093, USA

<sup>2</sup>Howard Hughes Medical Institute, Salk Institute for Biological Studies, La Jolla, CA 92037, USA

<sup>3</sup>Department of Neurobiology, Stanford University, Stanford, CA 94305, USA

<sup>4</sup>Volen Center and Biology Department, Brandeis University, Waltham, MA 02454, USA

<sup>5</sup>Division of Biological Sciences, University of California at San Diego, La Jolla, CA 92093, USA

\*Address correspondence to: [ahwillia@stanford.edu](mailto:ahwillia@stanford.edu), [toleary@brandeis.edu](mailto:toleary@brandeis.edu)

## ABSTRACT

Nervous system function depends on the appropriate development, maintenance, and plasticity of synaptic connectivity. In order to form and modify synaptic connections, organelles and molecular cargo need to be trafficked from the site of synthesis to the vicinity of the synapse. An open question is how synaptic cargo can be delivered to appropriate synapses in spite of the complex dendritic arbors and thousands of postsynaptic sites typical of many neurons. We develop a biophysically-rooted yet general model of microtubule transport that captures known mechanistic properties of intracellular transport. In spite of the assumption that molecular transport responds only to local chemical cues, we show that arbitrarily complex distributions of cargo can be achieved. However, the model reveals important tradeoffs that can be tested experimentally. We find that precise and flexible delivery of synaptic cargo requires the capture of synaptic cargo to occur on a slower timescale than the movement of cargo across the microtubule network. Tuning the transport parameters reveals that optimal solutions exist for specific distributions of synapses, but these solutions sensitively depend on the location as well as the number of synapses, suggesting that biological neurons face a compromise between flexibility of connectivity and efficacy in regulating synaptic function.

Keywords: Synaptic tagging hypothesis, LTP, Transport, Morphology

## INTRODUCTION

Neurons often have complex dendritic trees, reflecting the dense and structured synaptic connectivity that supports nervous system function. In order to maintain appropriate connectivity, or to alter it in response to changes in circuit activity, numerous enzymes and macromolecules must be repeatedly replenished and redistributed amongst a staggering number of synaptic contacts. Although the molecular machinery that solves this logistical problem is known in increasing detail [REFS], there are few attempts to quantify broadly how subcellular transport processes might constrain a neuron's ability to regulate its connectivity and synaptic function.

Transport along dendrites is mediated by motor proteins (kinesins and dyneins) that walk along microtubules, carrying cargo at a rate that far exceeds passive diffusion (Smith and Simmons, 2001) Others?. The mechanisms that detach and sequester cargo at specific places in dendrites are not fully understood, but are known to depend on local biochemical signals such as transient elevations in cyclic AMP or  $[Ca^{2+}]$  (Mironov, 2007; Wang and Schwarz, 2009), that are caused by synaptic activity or locally released growth factors from other cells. In this way, the proteins, scaffolding molecules and receptors that make up a postsynaptic site can be made available to alter an existing synapse or assemble a new synapse in the vicinity of a presynaptic partner. Not all aspects of synaptic plasticity require delivery of cargo from the soma. For example, some forms of long-term potentiation (LTP) depend on local protein synthesis and can function in isolated dendrites [REFS]. Nonetheless, components originating in the soma need to find their way to synapses in the first place, and in the long run, the mRNAs and the machinery that supports local biosynthesis needs to be replenished. Moreover, many long-lasting forms of synaptic plasticity are known to depend on anterograde transport of mRNAs (Kandel, 2001; Puthanveetil et al., 2008) and specific mRNAs are known to be selectively transported to regions of heightened synaptic activity (Steward et al., 1998; Steward and Worley, 2001; Moga et al., 2004) or to developing synaptic contacts (Lyles et al., 2006). These observations fit with the well-known synaptic tagging hypothesis (Frey and Morris, 1997), which proposes that synapses produce a biochemical 'tag' that signals a requirement for synaptic building blocks as part of the plasticity process.

The distribution of molecular cargo is partially controlled by a coarse addressing system in the localization sequences of 3'-untranslated regions of mRNAs – which, for example, control

whether mRNA is sequestered in the nucleus or into dendrites (Andreassi and Riccio, 2009). However, it is unclear whether a fine-scale, centralized addressing system, as exemplified by human-designed transport systems, is feasible or even desirable for neurons to implement. Other biological systems (e.g. ant colonies) utilize decentralized transport strategies, which emerge from simple, local decisions made by a distributed population of agents (Deneubourg et al., 1990). Such self-organizing systems often enjoy a number of advantageous properties – including scalability, flexibility, and fault-tolerance – and are therefore a current topic of substantial interest to engineers (Werfel et al., 2014; Rubenstein et al., 2014).

We develop a minimal biophysical model that can account for activity-dependent accumulation of molecular cargo at synaptic sites in realistic neuronal morphologies, and show how local biochemical signals can modify the movement and/or release of cargo to produce complex spatial patterns in a self-organizing fashion. However, the decentralized transport strategies we explore face unavoidable tradeoffs between the speed and precision of cargo delivery. Tuning the transport parameters reveals that while optimal solutions exist to balance this tradeoff, these solutions sensitively depend on the location as well as the number of synapses, suggesting that biological neurons must compromise between flexibility in connectivity and their ability to precisely regulate synaptic function.

## RESULTS

### Model description

Activation of synaptic receptors triggers downstream signalling cascades that can alter global gene expression [ref Greenberg, Bading, others] as well as modulating the trafficking and metabolism of molecular cargo locally [REFS]. [more on this] **move to intro?**

Transport along microtubules is mediated by kinesin and dynein motors, which mediate anterograde and retrograde transport, respectively (Hirokawa et al., 2010; Gagnon and Mowry, 2011). Cargo is often simultaneously bound to both forms of motor protein, resulting in stochastic back-and-forth movements with a net direction determined by the balance of opposing movements (Hancock, 2014; Buxbaum et al., 2014a) (Fig. 1A).

To obtain a general model that can accommodate variations in the biophysical details, we consider microtubule-based transport as a biased random walk along a one-dimensional cable

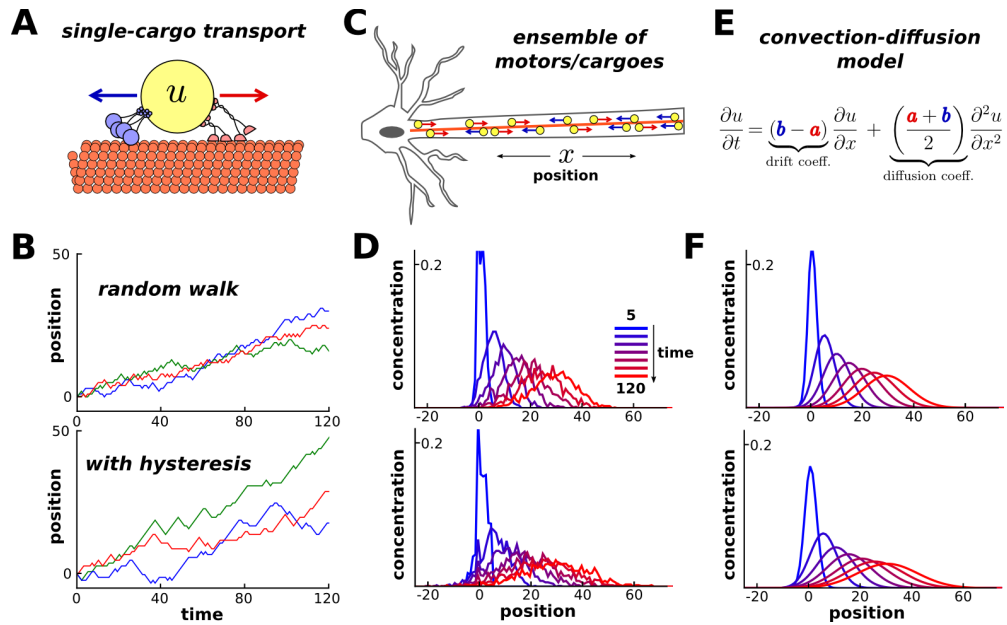


**Figure 1.** Model of microtubular transport. **(A)** Synaptic cargo,  $u$ , undergoes stochastic back-and-forth movements driven by opposing motor proteins. **(B)** Three example random walks on a cable representing the movement of individual cargoes. In a simple random walk, each movement is independent of previous movements (top panel); longer run lengths result from adding history-dependence to the model, such that each movement is likely to continue in the same direction as the previous step (bottom panel). **(C)** An ensemble of synaptic cargoes transported along the length of a neurite. **(D)** The concentration profile of transported cargo along a cable over time, simulated as 1,000 independent random walks. Simulations with (bottom) and without (top) history-dependence. **(E)** In the limit of many individual particles, the concentration of  $u$  is modeled by the convection-diffusion partial differential equation. The parameters,  $a$  and  $b$ , respectively scale the anterograde and retrograde rate of transport (see equation 1). **(F)** The convection-diffusion model provides a good fit for the simulations in panel D.

(Bressloff, 2006; Bressloff and Newby, 2009; Newby and Bressloff, 2010). For each time step, the cargo moves forwards, backwards, or remains in the same place with different probabilities that together sum to 1. In the simplest model, the probabilities associated with each movement are fixed and independent across each time step, with the forward jump more probable than a reverse jump, leading to a biased random walk (Fig. 1B, top panel). A potentially more realistic model (see, e.g., Soundararajan and Bullock (2014)) incorporates hysteresis into the biased random walk (see Methods). In this case, the cargo is more likely to continue in the same direction as it moved during the previous time step, leading to extended runs in one direction along the microtubule (Fig. 1B, bottom panel).

While the position of individual cargoes can be highly stochastic, the net movement of

a population of cargoes (Fig. 1C) is predictable. Figure 1D shows the distribution of 1000 molecules over time with (top panel) and without (bottom panel) hysteresis. For the simple biased random walk and for the random walk with hysteresis, these simulations can be well-fit by an advection-diffusion equation (Fig. 1E-F), which is easier to analyze because it is deterministic and contains fewer variables (Smith and Simmons, 2001).

We model transport using the advection-diffusion equation with spatially non-uniform drift and diffusion coefficients. As an approximation, we discretized a dendritic tree into small compartments, and modeled the movement of cargo between neighboring compartments as reactions with first order kinetics. In an unbranched cable with  $N$  compartments, the mass-action model is:



where  $u_i$  is the amount of cargo in each compartment, and  $a_i$  and  $b_i$  respectively denote local rate constants for anterograde and retrograde transport; these parameters determine the local diffusion and drift coefficients as shown in figure 1E (see Methods). Similar mass-action schemes can be constructed to model transport in branched morphologies (Fig. 2A). The mass-action scheme provides a flexible way to model local changes in transport rates, and is very tractable to mathematical analysis and numerical simulation.

A central assumption of mass-action description of this model is that the net movement of molecules between neighboring compartments is a stochastic and memoryless process. This assumption is reasonable for cargoes that change direction often; specifically, on a length scale comparable to the size of the compartments. This appears to be the case under many (Muller et al., 2008; Verbrugge et al., 2009), though not necessarily all (Dynes and Steward, 2007; Soundararajan and Bullock, 2014) circumstances. In simulations, we observed that this model was not very sensitive to violations of this assumption; the population dynamics of cargoes with substantial run lengths could still be well-fit by this class of models (Fig. 1F, lower panel; Supplementary Fig?).

### **A simple transport mechanism distributes cargo according to demand**

We next show how the mass-action model can be easily solved to produce complex distributions in the concentration of cargo along a dendrite. The exchange of  $u$  between neighboring compartments

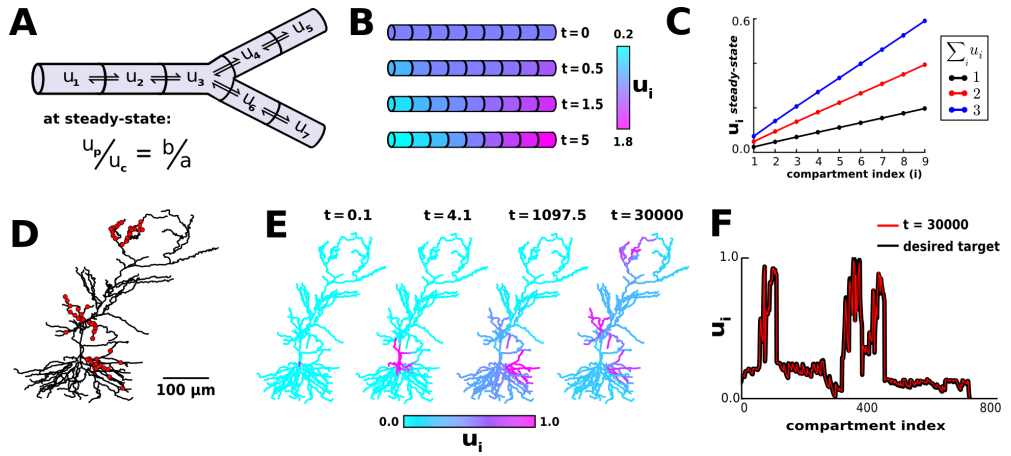


**Figure 2.** Local trafficking parameters determine the spatial distribution of biomolecules by a simple rule. **(A)** Diagram of the mass action transport model for a simple branched morphology. **(B)** A simulation of a nine compartment cable, with trafficking rate constants set to produce a linear gradient using the steady-state relation shown in panel A. **(C)** The slope of the linear gradient shown in panel B is determined by the total amount of  $u$  present in the model; the slope increases as more of  $u$  is present, but the linear profile is preserved. **(D)** A model of a CA1 pyramidal cell with 742 compartments based on Migliore and Migliore (2012); excitatory synapses were added at the locations marked by red dots. **(E)** The average membrane potential in each compartment of the CA1 model cell was used to define a desired spatial distribution, and transport rate constants were chosen according to equation (4). The desired spatial distribution of cargo emerges over time, after starting in the soma. **(F)** The desired and steady-state profile of  $u$  for each compartment in the simulation shown in panel E.

approaches an equilibrium/steady-state (ss) distribution over time. In an unbranched dendrite, this occurs precisely when:

$$\left. \frac{u_i}{u_{i+1}} \right|_{ss} = \frac{b_i}{a_i} \quad (2)$$

(see Methods). Thus, the local trafficking rates,  $a_i$  and  $b_i$ , can be tuned to produce a desired spatial distribution of cargo. Let  $\tilde{u}$  denote the desired steady-state level of  $u$  in each compartment. For example,  $\tilde{u}_i$  might refer to the local concentration of biochemical signal that “tags” synapses for plasticity (Frey and Morris, 1997); such a tag might be positively correlated to the desired level of delivered cargo. To match this desired distribution, the ratio of local trafficking rates should satisfy:

$$\frac{b_i}{a_i} = \frac{\tilde{u}_i}{\tilde{u}_{i+1}} \quad (3)$$

For example, a linear expression pattern emerges when  $\tilde{u}_i \propto i$ , resulting in  $b_i/a_i = i/i + 1$  (Fig. 2B). This rule produces the expected linear expression gradient with the slope controlled

by tuning the total amount of cargo in the cable (Fig. 2C).

These results extend directly to branched morphologies (see Methods). For any pair of connected compartments:

$$\frac{b}{a} = \frac{\tilde{u}_p}{\tilde{u}_c} \quad (4)$$

where  $u_p$  is the level in the “parent” compartment (closer to soma) and  $u_c$  is the level in the “child” compartment (closer to periphery);  $b$  and  $a$  refer to the local transport rate constants between this pair of compartments.

Together, this analysis shows that by slowing or biasing local trafficking rates, arbitrary distributions of cargo can be achieved over time. Local trafficking rates, in turn, can be modulated by a simple biochemical reaction resulting from synaptic activation or local release of a growth factor. We can consider the local cytoplasmic calcium concentration,  $[ca]_i$ , as an candidate second messenger. Increases in  $[ca]_i$  simultaneously arrest anterograde and retrograde microtubular transport (Wang and Schwarz, 2009). That is, for any pair of compartments, the anterograde rate constant is determined by calcium in the parent compartment,  $a = f([ca]_p)$ , and the retrograde rate constant is determined by calcium in the child compartment,  $b = f([ca]_c)$ , where  $f$  is a function that describes how calcium alters the transport rates. This results in:

$$\frac{b}{a} = \frac{f([ca]_c)}{f([ca]_p)} = \frac{\tilde{u}_p}{\tilde{u}_c} \quad (5)$$

where  $\tilde{u}_i = 1/f([ca]_i)$ .

Thus, in principle, local calcium transients that serve to arrest transport could provide a mechanism for matching cargo concentration to an arbitrarily complicated distribution over a dendritic tree. To test the plausibility of this model in a complex morphology, we extended an existing multi-compartment model of a CA1 pyramidal neuron (Migliore and Migliore, 2012). Excitatory synaptic input was delivered to 120 locations within three dendritic regions (red dots, Fig. 2D), and the average membrane potential in each electrical compartment determined the target level  $\tilde{u}_i$  in each compartment (Methods). This models how molecular cargo could be selectively trafficked to active synaptic sites. Figures 2E and 2F confirm that the spatial distribution of  $u$  approaches the desired steady-state.

## Convergence rate

Biochemical processes are time-sensitive. For example, newly synthesized proteins must be delivered to synapses within  $\sim 1$  hour to support long-term potentiation in CA1 pyramidal cells (Frey and Morris, 1997, 1998). It is therefore important to know what factors influence the rate at which the distribution of cargo matches its demand profile across the whole dendritic tree.

In equations (4) and (5), we implicitly required each  $\tilde{u}_i > 0$  in order to avoid division by zero. Intuitively, if  $\tilde{u}_i = 0$  for some compartment, then no cargo can flow through that compartment, cutting off more peripheral compartments from the transport system. Similarly, if certain  $\tilde{u}_i$  are nearly equal to zero, then transport through these compartments will act as a bottleneck for transport, and convergence to the desired distribution will be slow.

Figure 3 illustrates and analyzes a bottleneck in a simple three compartment model. The two compartments on the end of the cable have the same desired level,  $\tilde{u}_1 = \tilde{u}_3$ ; the middle compartment acts as a bottleneck when  $\tilde{u}_2$  is very small (Fig. 3A). This results in the mass-action model:



We assume that  $u$  begins at one end of the cable, and examine the how taking  $\varepsilon$  to zero affects the convergence rate. Figure 3B shows that the convergence rate slows dramatically as  $\varepsilon$  decreases. This can be solved by analysing the corresponding system of ordinary differential equations. The convergence rate is determined by the non-zero eigenvalue with smallest magnitude, which can be thought of as a rate-limiting step or process for the system (Methods, Supp. Fig. 1). Simulations confirmed this analysis and showed that the convergence rate diverges to infinity as  $\varepsilon$  approaches zero (Fig. 3C). I think the epsilon goes to zero stuff can be omitted, or at the very least stated more tersely - if the transport rate is zero anywhere it is obvious that it takes forever to converge

Qualitatively similar results were obtained in the multi-compartment CA1 neuron model. The model converged to a uniform target distribution more quickly than to a “bottleneck” target distribution, in which the middle third of the apical dendrite had low steady-state levels of cargo (Fig. 3D). Each pair of anterograde and retrograde rate constants were normalized to sum to one; thus, differences in convergence were not due to the scale of the trafficking rate constants.

In addition to this global view of convergence (Fig. 3D), we considered how the transport



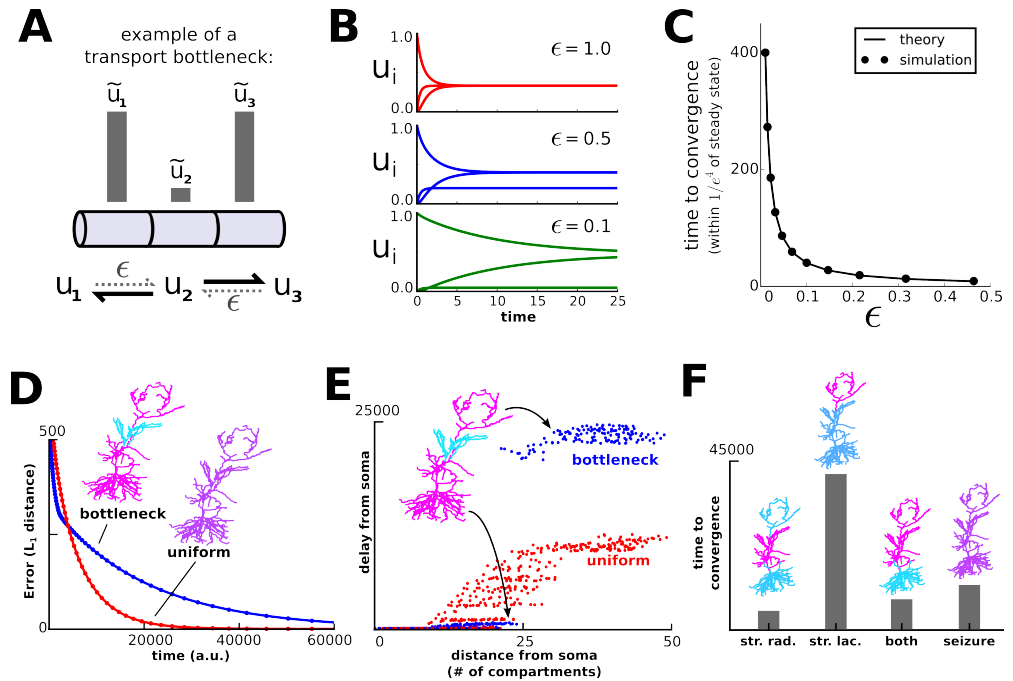


**Figure 3.** Convergence to steady-state is slow when molecules must be transported across bottlenecks —compartments with low target levels. **(A)** A three-compartment transport model, with the middle compartment acting as a bottleneck. The vertical bars represent the desired steady-state level of  $u$  in each compartment. The rate of transport into the middle compartment is small ( $\epsilon$ , dashed harpoons) relative to transport out of the middle compartment. **(B)** As  $\epsilon$  decreases, the model converges more slowly and the steady-state level decreases in the middle compartment. **(C)** Simulations (black dots) confirm that the time to convergence is given by the smallest non-zero eigenvalue of the system (analytically calculated line). This eigenvalue can be thought of as the rate-limiting step of the system. **(D)** Convergence ( $L_1$  distance) to a uniform target distribution (red line) is faster than a target distribution containing a bottleneck (blue line) in the CA1 model. **(E)** For all compartments that reach a threshold level ( $u_i = 0.001$ ), the simulated time it takes to reach threshold is plotted against the distance of that compartment to the soma. **(F)** Predicted convergence times for various target distributions (str. rad., stratum radiatum; str. lac., stratum lacunosum/moleculare).

bottleneck affected transport to individual dendritic compartments. Consider a scenario where transported cargo produces a local chemical reaction after a critical concentration threshold is reached; for example, a recently potentiated synapse might be stabilized after enough plasticity-related factors are delivered from the soma. Figure 3E plots the transport delay, or duration of time it took for  $u_i$  to reach a pre-defined threshold for each compartment. We observed qualitatively similar results for different threshold values (data not shown).

As expected, introducing a bottleneck caused much longer delays to compartments distal to that bottleneck (Fig. 3E, upper right portion of plot). Interestingly, the presence of a bottleneck

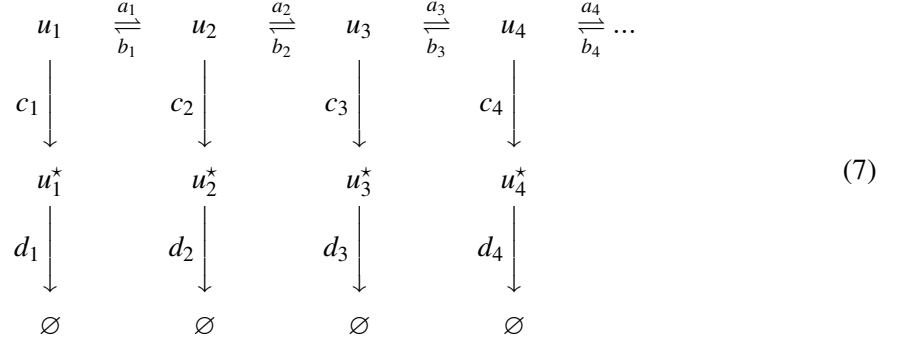
also *shortens* the transport delay to proximal compartments, compared to the uniform target distribution (Fig. 3E, lower left portion of plot). This occurs because cargo delayed by the bottleneck spreads throughout the proximal compartments, reaching higher levels earlier in the simulation.

One experimentally testable prediction of this analysis is that transport to distal compartments should be quickened by allowing higher levels of  $u$  into the proximal compartments at steady-state (Fig. 3E). This might be tested by characterizing the convergence time of a retrogradely transported molecule that aggregates at recently activated synapses, such as *Arc* mRNA (Steward et al. (1998), see discussion). To illustrate this in the model CA1 cell, we characterized the time course of transport to the distal apical dendrite (stimulating stratum lacunosum/moleculare), proximal apical dendrite (stimulating stratum radiatum), entire apical dendrite (stimulating both layers), and entire cell (seizure). Notably, the model converges more slowly to distal input alone, than to paired distal and proximal input, or to an entirely uniform input distribution (Fig. 3F).

### **Microtubular trafficking, detachment and degradation on separated time scales**

So far we have considered how local signals can generate a specific distribution of molecular cargo along a dendrite by modulating the rate of molecular motors. However, while certain types of molecular cargo stay on the microtubule network (e.g. mitochondria), many kinds of cargo must detach from the microtubules in order to be used at their final location. For example, dendritic mRNAs are transported along microtubules within densely-packed granules, and are released following granule disassembly (Krichevsky and Kosik, 2001; Buxbaum et al., 2014b). In this case, and in others where the cargo is disassembled or sequestered, it is reasonable to model detachment from the microtubule as an irreversible process, followed by an eventual degradation. We therefore model the detachment from the microtubule in the mass-action scheme as having a unidirectional rate constant, and include a compartment-specific degradation reaction. This

results in the following scheme:



As before, a molecule  $u$  is transported along a network of microtubules (top row, in equation 6). In each compartment, molecules can irreversibly detach from the microtubules in a reaction  $u_i \xrightarrow{c_i} u_i^*$ , where  $u^*$  denotes the biochemically active form of  $u$ , which is assumed to be inactive during transport. The final reaction,  $u_i^* \xrightarrow{d_i} \emptyset$ , models degradation in each compartment. Note that only  $u^*$  is subject to degradation; the molecule is assumed to be protected from degradation during transport. This model can be extended to branched morphologies (Fig. 3A).

One way to analyze this system is to assume that these three processes — trafficking, detachment, and degradation — occur on separate timescales. If trafficking is sufficiently faster than detachment ( $a, b \gg c$ ), then  $u$  approaches a quasi-steady state distribution defined by our previous analysis (equation 4). We then choose detachment rate constants that transform the microtubular distribution into our desired distribution for  $u^*$ :

$$c_i \propto \frac{\tilde{u}_i^*}{\tilde{u}_i} \tag{8}$$

Here,  $\tilde{u}$  and  $\tilde{u}^*$  respectively denote the quasi-steady state distributions for  $u$  and  $u^*$ , respectively. Due to the degradation reaction, the system no longer approaches a steady-state; however, as long as degradation is sufficiently slow ( $c \gg d$ ) the desired distribution is transiently achieved.

This model has a continuum of strategies for controlling the eventual distribution of molecular cargo (Fig. 4B). At one extreme of this continuum (Fig. 4C), microtubular trafficking rates are constrained such that  $\tilde{u}$  exactly matches  $\tilde{u}^*$ , and the detachment rate constants are spatially uniform ( $c_i = \text{constant}$ ). In this case, Figure 4C shows that the desired spatial distribution is achieved both along the microtubules (red line) and for the detached/activated cargo (blue line).

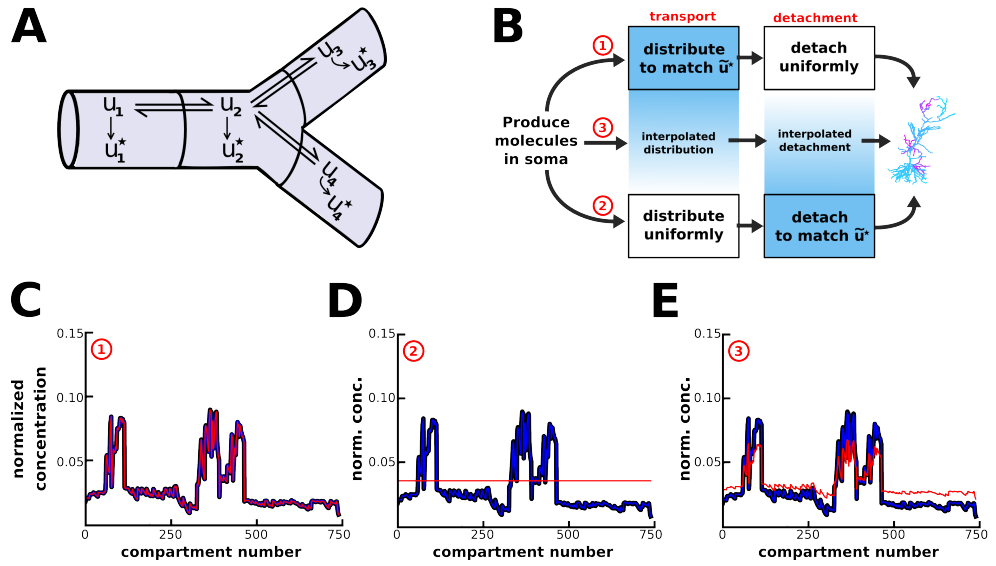


**Figure 4.** Multiple strategies for transport in a model including nonuniform microtubular detachment/activation. **(A)** Schematic of microtubular transport model with irreversible detachment in a branched morphology. The localized degradation reactions ( $u_i^* \xrightarrow{d_i} \emptyset$ ) is omitted. **(B)** Multiple strategies for producing a desired distribution of activated biomolecules ( $\tilde{u}^*$ ). When the timescale of detachment/delivery is sufficiently slow, the distribution of cargo on the microtubules approaches a quasi-steady-state (transport step). This known distribution can then be transformed into the desired distribution for  $\tilde{u}$  (detachment step). As long as these two steps are appropriately matched (blends of blue), then the desired distribution will be achieved (CA1 cell, right). **(C-E)** Normalized distributions of  $u$  (red),  $u^*$  (blue), and  $\tilde{u}^*$  (black) as  $t \rightarrow \infty$  for various strategies diagrammed in panel B (see circled red numbers).

The other extreme case is where trafficking rates are fixed along the microtubules, but cargo detaches in response to local signals at a rate proportional ( $c_i \propto \tilde{u}_i^*$ ). Figure 4D shows this strategy. Unlike the first solution, this strategy avoids the transport bottlenecks examined in Figure 3, and can achieve target patterns with  $\tilde{u}^*$  equal to zero in certain compartments by setting  $c_i = 0$ .

Figure 4E shows the behavior of an intermediate model, whose parameters are a linear interpolation between the extreme strategies shown in Figure 4C and 4D. Thus, effective trafficking systems can be achieved by a spectrum of strategies, which may be suited to different situations and purposes (see Discussion).

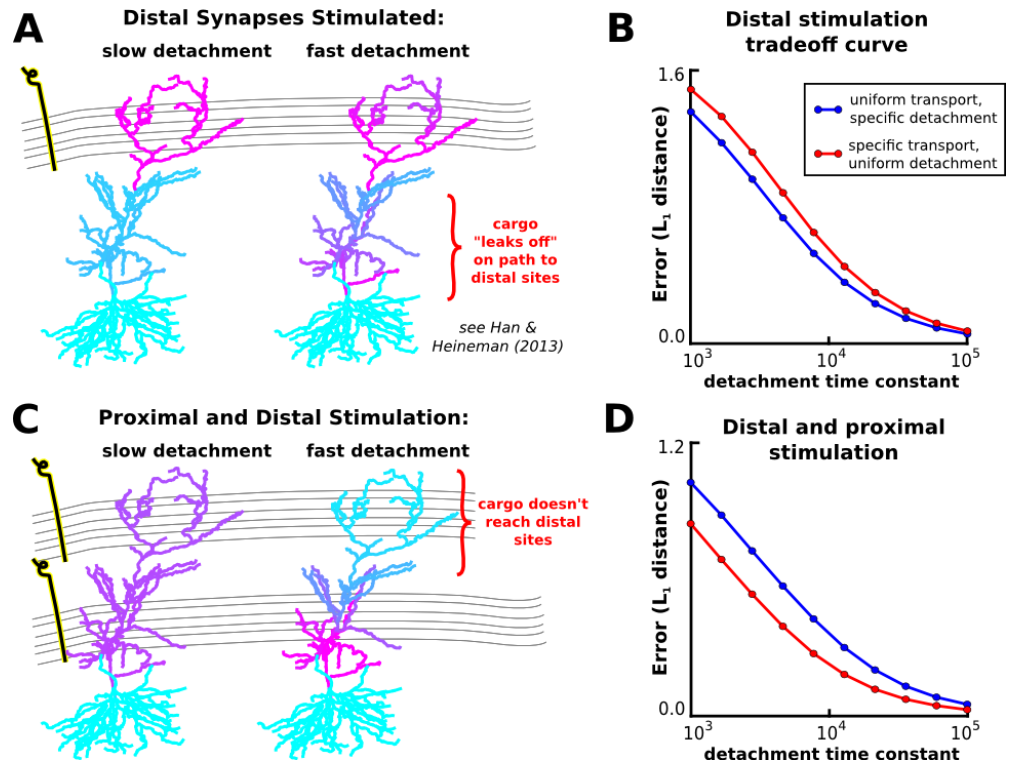


**Figure 5.** Proximal synapses capture more cargo at the expense of distal synapses when detachment rates are naïvely increased. (A) Delivery of cargo to the distal apical zone with slow (left) and fast detachment rates (right). The steady-state cargo distribution does not match the stimulated pattern when detachment is fast. (B) Tradeoff curves between non-specificity and convergence rate for two trafficking strategies (blue line, see Fig 4D; red line, see Fig 4C). (C-D) Same as (A-B) but for cargo delivery to the entire apical tuft.

### Non-specific cargo delivery occurs when trafficking and detachment occur on similar timescales

So far we have considered models that distribute cargo to high precision across a dendritic tree and found that high precision can be achieved when detachment is sufficiently slow relative to trafficking. However, biological neurons are unlikely to require perfect matching between demand and distribution of cargo and may therefore tolerate loss of precision in order to speed up delivery globally. We therefore examined the consequences of relaxing the separation of time scales between transport and detachment.

Returning to the model of Figure 4, we consider a scenario where distal synaptic inputs on the apical tuft are stimulated (Fig. 5A). If the average detachment rate constants are sufficiently slow, then, as before, cargo is delivered selectively to the stimulated region (Fig. 5A, left). If we increase the detachment rates by a uniformly scaling, some cargo “leaks off” the microtubule

path on its way to the distal synapses (Fig. 5A, right). We refer to this as a “non-specific” delivery of cargo, since cargo is not selectively delivered to the stimulated sites. Thus, although speeding up detachment relative to transport improves the overall rate at which cargoes are delivered to synapses, but this comes at the cost of decreased accuracy of delivery. For this stimulation pattern, non-specificity might induce on-the-path synaptic plasticity; a possibility that has some experimental evidence (Han and Heinemann, 2013).

Tradeoff curves between the average detachment rate constant and the non-specificity of transport for this stimulation pattern are shown in figure 5B. Importantly, this tradeoff exists for both trafficking strategies we examined in figure 4 — the selective transport strategy (see Fig 4D) and uniform transport strategy (see Fig. 4C). The uniform trafficking strategy (Fig. 5B, blue line) outperforms the specific trafficking strategy (Fig. 5B, red line) since the latter suffers from bottleneck in the proximal apical zone.

The pattern of non-specific delivery is stimulation-dependent. When the entire apical tree is stimulated, fast detachment can result in a complete occlusion of cargo delivery to distal synaptic sites (Fig. 5C). As before, a tradeoff between specificity and delivery speed is present for both transport strategies (Fig. 5D). Interestingly, the specific trafficking strategy outperforms the uniform trafficking strategy in this case (in contrast to Fig. 5A-B). This is due to the lack of a bottleneck, and the fact that the uniform trafficking strategy initially sends cargo to the basal dendrites where it is not released. Together, these results show that an increase in the efficiency of synaptic cargo delivery comes at the cost of loss of specificity and that the final destination of mis-trafficked cargo depends on the pattern of stimulation. We next asked whether we can tune the kinetic parameters of the transport mechanism to find an ideal compromise between precision and trafficking efficiency.

### **Transport can be optimized for both speed and precision for a given stimulation pattern**

In figure 5, we showed that scaling the detachment rates ( $c_i$ ), while leaving the transport rates ( $a_i, b_i$ ) fixed produces a proximal bias in cargo delivery. That is, synapses closer to the soma are more likely to capture cargo at the expense of distal synapses. We reasoned that increasing the anterograde transport rate of cargo could correct for this bias, producing transport rules that are both fast and precise.

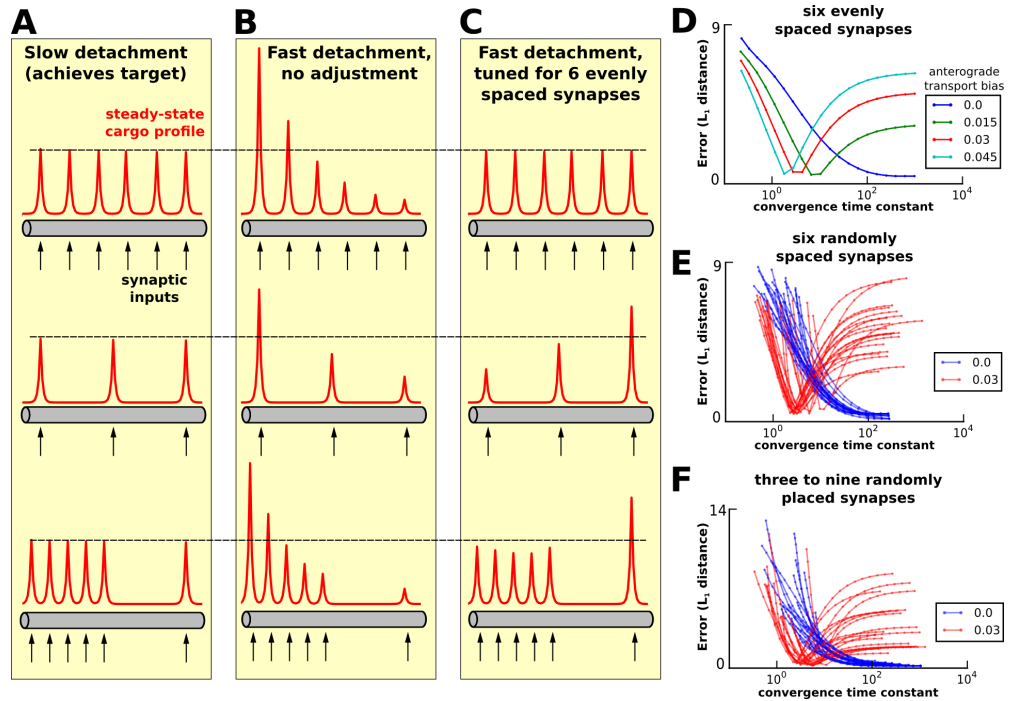


**Figure 6.** Producing speed and specificity for particular stimulation patterns does not extend to other patterns. Cargo begins on the left end and is transported to the right. **(A-C)** Steady-state cargo profiles (red) for three stimulation patterns (black arrows) along an unbranched cable. The dotted black line corresponds to the ‘target’ steady-state level at each synapse. **(A)** When the timescale of detachment is sufficiently slow, cargo can be evenly distributed to the synapses regardless of their number and position. Transport parameters were set according to the procedure shown in figure 4D. **(B)** When detachment is naïvely increased (all rates multiplicatively scaled) a proximal bias in the steady-state distribution of cargo across all stimulation patterns. **(C)** Transport rate constants,  $a_i$  and  $b_i$ , were tuned to optimize the distribution of cargo to six equally spaced synapses (top row); detachment rate constants were the same as in panel B. Changing the number of synapses (middle row) or the position of the synapses (bottom row) causes the unequal distribution of cargo to synapses. **(D)** Tradeoff curves between non-specificity and convergence rate for six evenly spaced synapses (top row of A-C). The curve shifts to the left and becomes non-monotonic as the anterograde bias ( $\beta$ ) increases. **(E)** Tradeoff curves for two levels of anterograde bias on multiple simulations; for each simulation six synapse positions were drawn from random uniform distribution over the length of the cable. **(F)** Same as panel E, except each the number of synapses was randomly chosen between 3 to 9 for each simulation.

We examined this possibility in a simpler model — an unbranched cable — so that we could develop simple heuristics that precisely achieve a desired distribution of cargo while minimizing the convergence time. In the reduced model, cargo begins on the left end of the cable and is transported to a number of synaptic sites, each of which is modeled as a double-exponential curve.

As before, cargo can be precisely delivered to a variety of stimulation patterns when the detachment rate is sufficiently slow (Fig. 6A); when the detachment rate is naïvely increased to speed up the rate of delivery, a proximal bias develops for all stimulation patterns (Fig. 6B). This bias is qualitatively exponential.

We then hand-tuned the transport rate constants to deliver equal cargo to six evenly spaced synaptic sites (top row of Fig. 6C). Specifically, we increased the anterograde rate constants ( $a_i$ ) and decreased the retrograde rate constants ( $b_i$ ) by a decreasing linear function of position so that  $a_{N-1} = b_{N-1}$  at the right side of the cable. On the left end of the cable, we set  $a_1 = 0.5 + \beta$  and  $b_1 = 0.5 - \beta$ , where  $\beta$  is the parameter controlling anterograde bias. Intuitively, this pushes cargo past the proximal synaptic sites more quickly, canceling out the exponential delivery bias induced by fast detachment.

However, this tuned transport model does not precisely deliver cargo for other stimulation patterns. When the number of synapses on the cable is decreased, a distal delivery bias is observed because too little cargo is released on the proximal portion of the cable (middle row, Fig. 6C). Even when the number of synapses is held constant, changing the position of the synapses can disrupt equal distribution of cargo. This is shown in the bottom row of figure 6C, where a distal bias again develops when the majority of activated synapses are positioned proximally. Thus, within the simple framework we've developed, the delivery of cargo can be tuned to achieve both precision and speed for a specified target distribution. However, non-specific cargo delivery occurs when different stimulation patterns are applied (assuming the transport parameters are not re-tuned).

To examine these observations over a larger range of stimulation patterns and transport parameters, we plotted tradeoff curves between delivery precision and speed. We first examined a cable with six evenly spaced delivery sites (same as top row of Fig. 6A-C). As before, a hard tradeoff between specificity and delivery speed exists for the untuned model (blue line in Fig. 6D, same transport rate constants as Fig. 6A and 6B). As the transport rate constants are tuned to increase anterograde movement, the optimal points along the tradeoff curve move to the left, representing faster transport times. However, the tradeoff curves also become nonmonotonic: the error (non-specificity) initially decreases as the detachment rate decreases, but begins to increase after a certain well-matched point. Points on the descending left branch of the curve represent



cargo distributions with proximal bias (detachment is too fast); points on the ascending right branch correspond to distal bias (detachment is too slow).

We observed qualitatively similar tradeoff curves for randomly positioned synapses (Fig. 6E), and for randomizing the number and position of synapses (Fig. 6F). There is substantial variability in the tradeoff curves in both cases, but particularly when randomizing the number of synaptic inputs. Notably, the untuned transport model (blue curves) always converge to zero error as the detachment rate decreases. Thus, for this model, it appears that the only way to achieve very precise and flexible transport is to have a slow detachment rate.

## DISCUSSION

A microscope image of a typical neuronal dendritic tree hints at the complex logistical task that the neuron must solve to maintain synapses and alter them, as appropriate, during development and learning. Synapses, such as the extensively-studied excitatory synapses of the mammalian nervous system, comprise hundreds of different proteins, including receptors, structural and anchoring proteins, and cytosolic signaling enzymes (Liu et al., 2014; Laßek et al., 2015). How do these components find their way to the synapse, and how do synapses that have varying demands for these components receive an appropriate supply?

A large and diverse corpus of research speaks to this question, and many reviews have crystallized, in words, a two-step model in which molecular cargo first samples the dendritic arbor by a noisy walk, before its eventual release or capture (Welte, 2004; Doyle and Kiebler, 2011; Buxbaum et al., 2014a, 2015). Both stages of transport are thought to be influenced by localized signaling pathways, rather than being pre-determined by a precise molecular address tagged in the soma. The signaling pathways affecting transport require further characterization and discovery; candidate second-messengers include calcium (Wang and Schwarz, 2009), ADP (Mironov, 2007), and microtubule-associated proteins (Soundararajan and Bullock, 2014).

We aimed to examine the validity and biological consequences of these conceptual models in computational and theoretical detail, while remaining agnostic to biophysical parameters that require further study. A primary question we asked was whether a transport system based on purely local rules was feasible, or whether a complex global addressing system was required. One might naïvely expect that elaborately branched dendritic morphologies obfuscate the relationship between local mechanisms and the global distribution of molecular cargo. However, we showed

that local rules can produce arbitrarily precise and flexible cargo delivery provided that the release of cargo occurs on a slow enough timescale. Intuitively, this requirement means that the cargo have time to sample the dendritic tree for potential delivery sites (Welte, 2004).

Importantly, the spatial sampling of cargo need not occur in a uniform or unbiased manner. We showed that the same distribution of cargo could be achieved by (a) nonuniform microtubular transport followed by uniform release, (b) from uniform transport followed by nonuniform release, or (c) a combination of these strategies (Fig. 4). Biologists should consider that dendritic transport may be better understood as a family of strategies, rather than a single mechanism or procedure. For example, Kim and Martin (2015) identified three mRNAs that were uniformly distributed throughout cultured *Aplysia* sensory neurons, but were targeted to synapses at the level of protein expression by localized translation. In contrast, the nonuniform expression of *Arc* mRNA is closely matched to the pattern of Arc protein (Farris et al., 2014; Steward et al., 2015). Even the same molecular cargo can show diverse movement statistics in single-particle tracking experiments (Dynes and Steward, 2007) Others?.

Different transport strategies might be tailored for different constraints or purposes. One experimentally testable prediction of the model is that bottlenecks can arise when cargo is transported nonuniformly; specifically when distal regions require high levels of cargo, while proximal regions require low levels (Fig. 3). Uniformly distributing cargo and relying on local capture circumvents this problem, leading to faster convergence for certain target distributions of cargo. An additional consideration, not examined in detail here, is whether the distribution of cargo needs to be stable over long time periods or be dynamic and responsive to changes in synaptic input. We also focused our analysis on the transport of transiently expressed cargo (e.g. factors produced in response to high synaptic input), rather than cargo that is constitutively expressed and, in some cases, differentially captured or synthesized across the dendritic tree (CITE). However, much of our analysis would extend to this case.

The slow delivery/capture of cargo can produce a well-behaved and predictable transport system that can be flexibly tuned by simple local mechanisms and is not sensitive to the complex geometry of the neuron. Mathematically, this regime occurs when the system contains two separated timescales, and the distribution of cargo along the microtubules approaches a quasi-steady-state. However, because the transport of certain cargoes is time-sensitive (Frey and

Morris, 1997, 1998), we asked whether the model could maintain precise delivery while relaxing the restriction of slow detachment. We found that increasing the rate of detachment produces a proximal bias in the delivery of cargo; this behavior, while intuitive at a high level, is complex and difficult to analytically characterize in complex morphologies. Thus, the family of models based on quasi-steady-state approximation predicts a tradeoff between the speed of cargo delivery and the specificity of transport.

We then asked whether a different family of models might circumvent this tradeoff by globally tuning the anterograde and retrograde movement rates. Inspired by studies showing that a directional bias in transport can be induced by changing the complement of motor proteins (Kanai et al., 2004; Amrute-Nayak and Bullock, 2012), and that such a change might be induced at the soma in response to synaptic activity (Puthanveetil et al., 2008), we increased the anterograde transport rates in a simple model to precisely overcome the proximal bias in cargo delivery, and therefore provide both fast and precise transport for a particular target distribution of cargo (Fig. 6).

There are three important facts to emphasize about this globally tuned solution. First, we achieved precise delivery when the anterograde rate constants were tuned non-uniformly over the cable; specifically, we used a linearly decreasing profile (see *Methods*). Simply changing the composition of motor proteins (Amrute-Nayak and Bullock, 2012) may be insufficient to induce a spatial profile in transport bias; non-uniform modulation of the microtubule network or expression of microtubule-associated proteins provide potential mechanisms (Kwan et al., 2008; Soundararajan and Bullock, 2014). While these biophysical details remain speculative, single-particle tracking studies could empirically test the existence of spatial gradients in anterograde movement bias.

Secondly, it should be emphasized that the linear, decreasing gradient in anterograde bias used in figure 6 is not a general prediction for all neuronal morphologies or detachment/capture profiles. Introducing an anterograde bias can cause the accumulation of cargo at the tips of short branches, proximal to the soma (data not shown). While the optimal re-tuning of transport rate constants is morphology-dependent, the qualitative prediction that anterograde bias should decrease as a function of distance to the soma is likely general. Intuitively, the anterograde bias should be low near the tips of the dendritic branches to prevent the accumulation of

cargo. However, other mechanisms, not modeled in this study, might prevent this accumulation (Soundararajan and Bullock, 2014).

Finally, and perhaps most importantly, the optimal re-tuning of anterograde transport bias depends on the number and pattern of delivery sites (see Fig. 6). If neurons are able to consistently circumvent the tradeoff between delivery speed and precision, then the model predicts that they must globally re-tune transport rates in a pattern-specific manner.

Need a nice final paragraph to tie it all together

## METHODS

All simulation code is available on: <https://github.com/ahwillia/Williams-et-al-Synaptic-Transport>

### Model of single-particle transport

Let  $x_n$  denote the position of a particle along a 1-dimensional cable at timestep  $n$ . Let  $v_n$  denote the velocity of the particle at timestep  $n$ ; for simplicity, we assume the velocity can take on three discrete values,  $v_n = \{-1, 0, 1\}$ , corresponding to a discrete retrograde movement, pause, or anterograde movement. As a result,  $x_n$  is constrained to take on integer values. In the memoryless transport model (top plots in Fig. 1B, 1D, and 1F), we assume that  $v_n$  is drawn with fixed probabilities on each step. The update rule for position is:

$$x_{n+1} = x_n + v_n$$

$$v_{n+1} = \begin{cases} -1 & \text{with probability } p_- \\ 0 & \text{with probability } p_0 \\ 1 & \text{with probability } p_+ \end{cases}$$

We chose  $p_- = 0.2$ ,  $p_0 = 0.35$  and  $p_+ = 0.45$  for the illustration shown in Figure 1. For the model with history-dependence (bottom plots in Fig. 1B, 1D, and 1F), the movement probabilities at each step depend on the previous movement. For example, if the motor was moving in an anterograde direction on the previous timestep, then it is more likely to continue to moving in

that direction in the next time step. In this case the update rule utilizes *conditional* probabilities:

$$v_{n+1} = \begin{cases} -1 & \text{with probability } p(-|v_n) \\ 0 & \text{with probability } p(0|v_n) \\ 1 & \text{with probability } p(+|v_n) \end{cases}$$

In the extreme case of history-dependence, the particle always steps in the same direction as the previous time step.

	$v_n = -1$	$v_n = 0$	$v_n = 1$
$p(v_{n+1} = -1)$	1	0	0
$p(v_{n+1} = 0)$	0	1	0
$p(v_{n+1} = 1)$	0	0	1

We introduce a parameter  $k \in [0, 1]$  to linearly interpolate between this extreme case and the memoryless model. The rest of the panels in the figure show individual runs, 5000 molecule simulations, and mass action approximations for  $k = 0.5$ .

### Model of bulk/mass-action transport

Transport in an unbranched cable (equation 1) leads to the following system of differential equations:

$$\begin{aligned} \dot{u}_1 &= -a_1 u_1 + b_1 u_2 \\ \dot{u}_2 &= a_1 u_1 - (a_2 + b_1) u_2 + b_2 u_3 \\ &\vdots \\ \dot{u}_i &= a_{i-1} u_{i-1} - (a_i + b_{i-1}) u_i + b_i u_{i+1} \\ &\vdots \\ \dot{u}_N &= a_{N-1} u_{N-1} - b_{N-1} u_N \end{aligned}$$

Similar systems result from branched mass-action models. The steady-state ratio of cargo in two neighboring compartments equals the ratio of transport rate constants (equation 2). This can be immediately verified at either end of the cable:

$$\dot{u}_1 = 0 \Rightarrow -a_1 u_1 + b_1 u_2 = 0 \Rightarrow \left. \frac{u_1}{u_2} \right|_{ss} = \frac{b_1}{a_1}$$

Successively applying the same logic down the cable confirms the condition in equation 2 holds globally. A similar procedure (starting at the tips and moving in) can be applied to branched morphologies to prove the more general condition (equation 4).

It is helpful to re-express the model as a matrix differential equation,  $\dot{\mathbf{u}} = A\mathbf{u}$ , where  $\mathbf{u} = [u_1, u_2, \dots, u_N]^T$  is the state vector, and  $A$  is the state-transition matrix. For a general branched morphology,  $A$  will be nearly tridiagonal, with off-diagonal elements corresponding to branch points; matrices in this form are called Hines matrices (Hines, 1984). For the simpler case of an unbranched cable,  $A$  is tridiagonal:

$$A = \begin{bmatrix} -a_1 & b_1 & 0 & & \dots & 0 \\ a_1 & -b_1 - a_2 & b_2 & 0 & & \\ 0 & a_2 & -b_2 - a_3 & b_3 & \ddots & \vdots \\ \vdots & 0 & a_3 & \ddots & & 0 \\ & & \ddots & & -b_{N-2} - a_{N-1} & b_{N-1} \\ 0 & & \dots & 0 & a_{N-1} & -b_{N-1} \end{bmatrix}$$

For both branched and unbranched morphologies, each column of  $A$  sums to zero, which reflects conservation of mass within the system. The rank of  $A$  is exactly  $N - 1$  (this can be seen by taking the sum of the first  $N - 1$  rows, which results in  $-1$  times the final row). Thus, the nullspace of  $A$  is one-dimensional (red lines in Supp. Fig. 1).

The desired steady-state distribution,  $\tilde{\mathbf{u}}$ , is an eigenvector that spans the nullspace of  $A$ . It is simple to show that all other eigenvalues  $A$  are negative using the Gershgorin circle theorem; thus, the fixed point described by equations 2 and 4 is stable. The convergence rate is determined by the non-zero eigenvalue with smallest magnitude of  $A$ .

### Stochastic Interpretation of Mass-Action Model

The mass-action model described in figure 2 is a deterministic dynamical system. However, this determinism only holds in the limit of having a very large number of transported particles. Cargoes with small copy numbers (e.g. mitochondria) will operate in a stochastic regime. We evoke a standard assumption that the system is *ergodic*, meaning that position of one particle averaged over very long time intervals is the same as the ensemble steady-state distribution.

Thus, in addition to modeling how the spatial distribution of cargo changes over time, the

mass-action model equivalently models the spatial probability distribution of a single cargo. That is, imagine we track a single cargo and ask its position after a long period of transport. The probability ratio between of finding this particle in any parent-child pair of compartments converges to:

$$\left. \frac{p_p}{p_c} \right|_{ss} = \frac{b}{a}$$

which mirrors our analysis of the deterministic model.

At steady-state, the number of molecules in any single compartment follows a binomial distribution; the coefficient of variation in each compartment is given by:

$$\sqrt{\frac{1 - p_i^{(ss)}}{n p_i^{(ss)}}}$$

This suggests that there are two ways of decreasing noise in the system. First, increasing the number of transported molecules,  $n$ , decreases the noise by a factor of  $1/\sqrt{n}$ . Additionally, transport is more reliable to compartments with a high steady-state occupation probability.

### Detachment and Degradation Reactions and Quasi-Steady-State Approximation

Introducing detachment and degradation reactions into the transport model is straightforward.

For an arbitrary compartment in a cable, the differential equations become:

$$\begin{aligned}\dot{u}_i &= a_{i-1}u_{i-1} - (a_i + b_{i-1} + c_i)u_i + b_i u_{i+1} \\ \dot{u}_i^* &= c_i u_i - d_i u_i^*\end{aligned}$$

When  $a_i, b_i \gg c_i \gg d_i$ , then the variables  $u_i$  and  $u_i^*$  approach a quasi-steady-state, which we denote  $\tilde{u}_i$  and  $\tilde{u}_i^*$ . We present two strategies for achieving a desired distribution for  $\tilde{u}_i^*$  in figure 4C and 4D. To interpolate between these strategies, let  $F$  be a scalar between 0 and 1, and let  $\tilde{u}^*$  be normalized to sum to one. We choose  $a_i$  and  $b_i$  to achieve:

$$\tilde{u}_i = F \tilde{u}_i^* + (1 - F)/N$$

along the microtubular network and choose  $c_i$  to satisfy

$$c_i \propto \frac{\tilde{u}_i^*}{F \tilde{u}_i^* + (1 - F)/N}$$

Here,  $N$  is the number of compartments in the model. Setting  $F = 1$  results in the simulation in figure 4C, while setting  $F = 0$  results in the simulation in figure 4D. An interpolated strategy is shown in figure 4E ( $F = 0.3$ ).

## ACKNOWLEDGEMENTS

## REFERENCES

- Amrute-Nayak, M. and Bullock, S. L. (2012). Single-molecule assays reveal that rna localization signals regulate dynein-dynactin copy number on individual transcript cargoes. *Nature cell biology*, 14(4):416–423.
- Andreassi, C. and Riccio, A. (2009). To localize or not to localize: mrna fate is in 3 utr ends. *Trends in cell biology*, 19(9):465–474.
- Bressloff, P. and Newby, J. (2009). Directed intermittent search for hidden targets. *New J. Phys.*, 11(2):023033.
- Bressloff, P. C. (2006). Stochastic model of protein receptor trafficking prior to synaptogenesis. *Physical Review E*, 74(3).
- Buxbaum, A. R., Haimovich, G., and Singer, R. H. (2014a). In the right place at the right time: visualizing and understanding mRNA localization. *Nature Reviews Molecular Cell Biology*, 16(2):95–109.
- Buxbaum, A. R., Wu, B., and Singer, R. H. (2014b). Single-Actin mRNA Detection in Neurons Reveals a Mechanism for Regulating Its Translatability. *Science*, 343(6169):419–422.
- Buxbaum, A. R., Yoon, Y. J., Singer, R. H., and Park, H. Y. (2015). Single-molecule insights into mrna dynamics in neurons. *Trends in cell biology*, 25(8):468–475.
- Deneubourg, J.-L., Aron, S., Goss, S., and Pasteels, J. M. (1990). The self-organizing exploratory pattern of the argentine ant. *Journal of insect behavior*, 3(2):159–168.
- Doyle, M. and Kiebler, M. A. (2011). Mechanisms of dendritic mRNA transport and its role in synaptic tagging. *The EMBO Journal*, 30(17):3540–3552.
- Dynes, J. L. and Steward, O. (2007). Dynamics of bidirectional transport of *Arc* mRNA in neuronal dendrites. *J. Comp. Neurol.*, 500(3):433–447.
- Farris, S., Lewandowski, G., Cox, C. D., and Steward, O. (2014). Selective Localization of *Arc* mRNA in Dendrites Involves Activity- and Translation-Dependent mRNA Degradation.



- Journal of Neuroscience*, 34(13):4481–4493.
- Frey, U. and Morris, R. (1998). Weak before strong: dissociating synaptic tagging and plasticity-factor accounts of late-LTP. *Neuropharmacology*, 37(4-5):545–552.
- Frey, U. and Morris, R. G. M. (1997). Synaptic tagging and long-term potentiation. *Nature*, 385(6616):533–536.
- Gagnon, J. and Mowry, K. (2011). Molecular motors: directing traffic during RNA localization. *Crit Rev Biochem Mol Biol*, 46:229–39.
- Han, E. B. and Heinemann, S. F. (2013). Distal Dendritic Inputs Control Neuronal Activity by Heterosynaptic Potentiation of Proximal Inputs. *Journal of Neuroscience*, 33(4):1314–1325.
- Hancock, W. O. (2014). Bidirectional cargo transport: moving beyond tug of war. *Nature Reviews Molecular Cell Biology*, 15(9):615–628.
- Hines, M. (1984). Efficient computation of branched nerve equations. *Int J Biomed Comput*, 15(1):69–76.
- Hirokawa, N., Niwa, S., and Tanaka, Y. (2010). Molecular Motors in Neurons: Transport Mechanisms and Roles in Brain Function Development, and Disease. *Neuron*, 68(4):610–638.
- Kanai, Y., Dohmae, N., and Hirokawa, N. (2004). Kinesin transports rna: isolation and characterization of an rna-transporting granule. *Neuron*, 43(4):513–525.
- Kandel, E. R. (2001). The Molecular Biology of Memory Storage: A Dialogue Between Genes and Synapses. *Science*, 294(5544):1030–1038.
- Kim, S. and Martin, K. C. (2015). Neuron-wide RNA transport combines with netrin-mediated local translation to spatially regulate the synaptic proteome. *eLife*, 4.
- Krichevsky, A. M. and Kosik, K. S. (2001). Neuronal RNA Granules A Link between RNA Localization and Stimulation-Dependent Translation. *Neuron*, 32(4):683–696.
- Kwan, A. C., Dombeck, D. A., and Webb, W. W. (2008). Polarized microtubule arrays in apical dendrites and axons. *Proceedings of the National Academy of Sciences*, 105(32):11370–11375.
- Laßek, M., Weingarten, J., and Volkhardt, W. (2015). The synaptic proteome. *Cell and tissue research*, 359(1):255–265.
- Liu, X.-A., Kadakkuzha, B., Pascal, B., Steckler, C., Akhmedov, K., Yan, L., Chalmers, M., and Puthanveetil, S. V. (2014). New approach to capture and characterize synaptic proteome. *Proceedings of the National Academy of Sciences*, 111(45):16154–16159.

- Lyles, V., Zhao, Y., and Martin, K. C. (2006). Synapse Formation and mRNA Localization in Cultured Aplysia Neurons. *Neuron*, 49(3):349–356.
- Migliore, M. and Migliore, R. (2012). Know your current  $i_h$ : Interaction with a shunting current explains the puzzling effects of its pharmacological or pathological modulations. *PLoS ONE*, 7(5):e36867.
- Mironov, S. L. (2007). ADP Regulates Movements of Mitochondria in Neurons. *Biophysical Journal*, 92(8):2944–2952.
- Moga, D., Calhoun, M., Chowdhury, A., Worley, P., Morrison, J., and Shapiro, M. (2004). Activity-regulated cytoskeletal-associated protein is localized to recently activated excitatory synapses. *Neuroscience*, 125(1):7–11.
- Muller, M. J. I., Klumpp, S., and Lipowsky, R. (2008). Tug-of-war as a cooperative mechanism for bidirectional cargo transport by molecular motors. *Proceedings of the National Academy of Sciences*, 105(12):4609–4614.
- Newby, J. and Bressloff, P. C. (2010). Local synaptic signaling enhances the stochastic transport of motor-driven cargo in neurons. *Physical biology*, 7(3):036004.
- Puthanveetil, S. V., Monje, F. J., Miniaci, M. C., Choi, Y.-B., Karl, K. A., Khandros, E., Gawinowicz, M. A., Sheetz, M. P., and Kandel, E. R. (2008). A New Component in Synaptic Plasticity: Upregulation of Kinesin in the Neurons of the Gill-Withdrawal Reflex. *Cell*, 135(5):960–973.
- Rubenstein, M., Cornejo, A., and Nagpal, R. (2014). Programmable self-assembly in a thousand-robot swarm. *Science*, 345(6198):795–799.
- Smith, D. and Simmons, R. (2001). Models of Motor-Assisted Transport of Intracellular Particles. *Biophysical Journal*, 80(1):45–68.
- Soundararajan, H. C. and Bullock, S. L. (2014). The influence of dynein processivity control, maps, and microtubule ends on directional movement of a localising mrna. *eLife*, 3.
- Steward, O., Farris, S., Pirbhoy, P. S., Darnell, J., and Driesche, S. J. V. (2015). Localization and local translation of Arc/Arg3.1 mRNA at synapses: some observations and paradoxes. *Front. Mol. Neurosci.*, 7.
- Steward, O., Wallace, C., Lyford, G., and Worley, P. (1998). Synaptic Activation Causes the mRNA for the IEG Arc to Localize Selectively near Activated Postsynaptic Sites on Dendrites.

*Neuron*, 21(4):741–751.

Steward, O. and Worley, P. F. (2001). Selective Targeting of Newly Synthesized Arc mRNA to Active Synapses Requires NMDA Receptor Activation. *Neuron*, 30(1):227–240.

Verbrugge, S., van den Wildenberg, S. M., and Peterman, E. J. (2009). Novel Ways to Determine Kinesin-1's Run Length and Randomness Using Fluorescence Microscopy. *Biophysical Journal*, 97(8):2287–2294.

Wang, X. and Schwarz, T. L. (2009). The Mechanism of  $Ca^{2+}$ -Dependent Regulation of Kinesin-Mediated Mitochondrial Motility. *Cell*, 136(1):163–174.

Welte, M. A. (2004). Bidirectional transport along microtubules. *Current Biology*, 14(13):R525–R537.

Werfel, J., Petersen, K., and Nagpal, R. (2014). Designing collective behavior in a termite-inspired robot construction team. *Science*, 343(6172):754–758.